

# Chemical Science

Accepted Manuscript

This article can be cited before page numbers have been issued, to do this please use: J. Yue, C. Yang, Y. Zhang, Q. Xiong and W. Luo, *Chem. Sci.*, 2025, DOI: 10.1039/D5SC02884A.



This is an Accepted Manuscript, which has been through the Royal Society of Chemistry peer review process and has been accepted for publication.

Accepted Manuscripts are published online shortly after acceptance, before technical editing, formatting and proof reading. Using this free service, authors can make their results available to the community, in citable form, before we publish the edited article. We will replace this Accepted Manuscript with the edited and formatted Advance Article as soon as it is available.

You can find more information about Accepted Manuscripts in the [Information for Authors](#).

Please note that technical editing may introduce minor changes to the text and/or graphics, which may alter content. The journal's standard [Terms & Conditions](#) and the [Ethical guidelines](#) still apply. In no event shall the Royal Society of Chemistry be held responsible for any errors or omissions in this Accepted Manuscript or any consequences arising from the use of any information it contains.

## ARTICLE

## Interstitial Nitrogen Modified Rh Nanocrystal for Efficient and CO-Resistant Alkaline Hydrogen Oxidation Electrocatalysis

Jianchao Yue, Chaoyi Yang, Yu Zhang, Qianqian Xiong, and Wei Luo\*

Received 00th January 20xx,  
Accepted 00th January 20xx

DOI: 10.1039/x0xx00000x

The preparation of active and CO-tolerant platinum-free electrocatalysts toward hydrogen oxidation reaction (HOR) under alkaline condition is significant for the practical development of anion exchange membrane fuel cells. Herein, nitrogen atoms intercalated into the interstitial void of rhodium (N-Rh/C) nanocrystal is fabricated, which constructs electron-deficient and electron-rich Rh sites simultaneously to coordinate the binding energies of multiple key intermediates, achieving highly active and CO-resistant alkaline HOR. In situ surface-enhanced infrared absorption spectroscopy and density functional theory calculations illustrate that the introduction of interstitial N atoms suppresses the electronic back-donation from Rh 4d to the CO  $2\pi^*$  orbital in electron-deficient sites, thereby weakening the CO adsorption and improving CO resistance. Additionally, the enhanced OH adsorption in electron-rich sites can release more free water into adjacent gap region, increasing water connectivity and hydrogen-bond networks in the electrical double layer, accelerating alkaline HOR kinetics.

## Introduction

Hydrogen fuel cell has garnered considerable attention in addressing the pressing issues of energy crises and environmental pollution.<sup>1-3</sup> The advancement of non-noble metal-based catalysts in alkaline environments significantly mitigates the reliance on precious metals in the cathodic oxygen reduction reaction (ORR), positioning anion exchange membrane fuel cells (AEMFCs) as one of the ideal devices.<sup>4-7</sup> However, the kinetics under alkaline conditions has decreased by several orders of magnitude compared to acidic conditions for the hydrogen oxidation reaction (HOR), which has observably hindered the large-scale application of AEMFCs.<sup>8,9</sup> Furthermore, hydrogen produced by current industrial methods inevitably contains a certain amount of CO, and purification will lead to a substantial increase in costs.<sup>10-12</sup> The reason for the poisoning and deactivation of active sites caused by CO adsorption is the strong electronic back-donation behavior from metal d to the CO  $2\pi^*$  orbitals.<sup>13</sup> Therefore, current research focuses on weakening the chemical CO adsorption by modulating the electronic structure of the catalyst.<sup>14-18</sup> However, it remains challenging to prepare alkaline HOR catalysts that simultaneously satisfy high activity and CO tolerance.

At present, the d-band center theory is mainly relied upon to describe the binding strength between various intermediates and the catalyst surface, and its downward shift is considered to reflect the weakening of intermediate adsorption.<sup>19,20</sup> However, for electrocatalytic processes involving multiple reactants, single-type electronic regulation of the catalyst is far

from sufficient. For instance, the downward shift of the metal d-band center will reduce the binding energy of H and CO, which is conducive to alkaline HOR, but will lead to a attenuated OH binding energy concurrently.<sup>21,22</sup> It has been reported that enhancing hydroxyl binding energy (OHBE) can promote the oxidation of surface-adsorbed H and CO and accelerate the HOR process.<sup>23,24</sup> Besides, Chen and his colleagues propose that the hydrogen-bond network in the electrical double layer (EDL) during alkaline hydrogen electrode reactions becomes sparse (i.e., there is a gap region) due to the presence of bulky cations, while OH adsorption can increase the  $H_2O_{gap}$  content, enhance the connectivity of the water network, and thereby promote the transport of  $H^+$ .<sup>25</sup> However, adjusting the metal active sites purposefully according to the adsorption requirements of different intermediates to achieve simultaneous optimization of binding strength is indispensable but also challenging for constructing excellent alkaline HOR catalysts.

Unlike traditional alloying and doping, interstitial alloying can change the electronic structure of metals without affecting the surface reaction of the catalyst, and can make full use of active sites.<sup>26-29</sup> Herein, we have successfully constructed interstitial N modified Rh supported on carbon (N-Rh/C) through colloidal synthesis and hydrothermal methods. DFT calculation results show that when the N atoms are inserted into the interstitial sites of Rh nanocrystals, and the CO\*/H\* adsorption site becomes electron-deficient while the OH\* adsorption site becomes electron-rich, thus simultaneously optimizing the adsorption of multiple intermediates. In situ surface-enhanced infrared absorption spectroscopy (SEIRAS) indicates that the N-Rh/C suppresses the electronic back-donation from Rh 4d to the CO  $2\pi^*$  orbital, thereby weakening the CO adsorption. Moreover, enhanced OH adsorption promotes the transformation of the interfacial water type, increasing the water content in the gap region and improving the connectivity

College of Chemistry and Molecular Sciences, Wuhan University, Wuhan, Hubei 430072, P. R. China. Email: wluo@whu.edu.cn  
Electronic Supplementary Information (ESI) available: See DOI: 10.1039/x0xx00000x



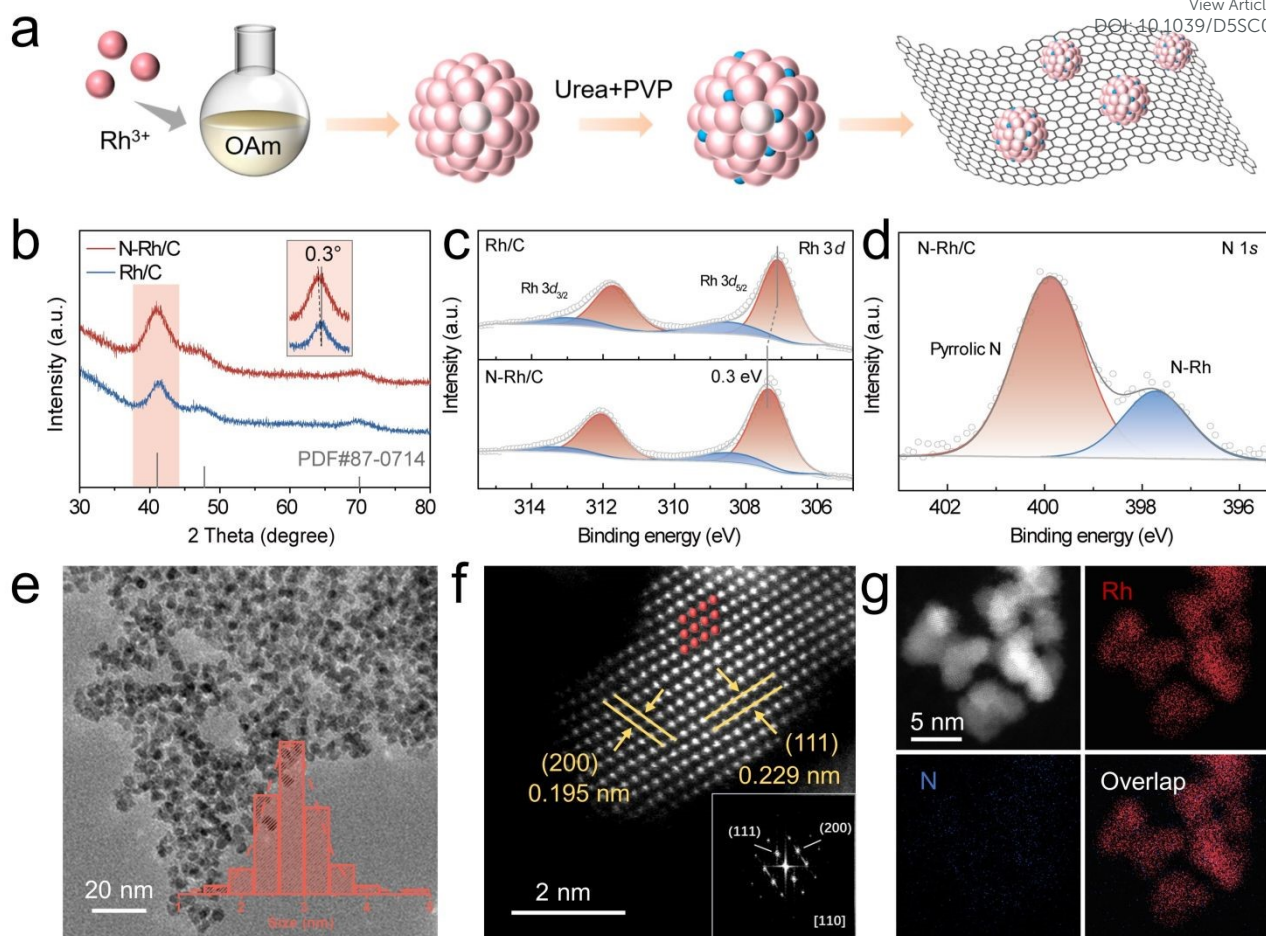


**Fig. 1** (a) The synthesis process diagram for N-Rh/C. (b) XRD patterns of N-Rh/C and Rh/C. (c) The Rh 3d XPS spectra for N-Rh and Rh/C. (d) XPS spectra of N 1s in N-Rh. (e) TEM image of the N-Rh. The inset shows the average size of the particles. (f) HAADF-STEM image of the N-Rh. The inset shows the corresponding FFT diffraction pattern of N-Rh. (g) HAADF-STEM elemental mappings of the N-Rh with Rh (red), N (blue), and overlap.

of the interfacial water network within the EDL. Consequently, N-Rh/C exhibits excellent alkaline HOR catalytic activity and CO tolerance, with a mass activity is 8.0 times higher than that of Rh/C and 2.7 times higher than that of Pt/C, respectively

## Results and discussion

The synthesis schematic diagram illustrates the general synthetic process for N-Rh/C in Fig. 1a, which first obtained Rh nanoparticles by colloidal synthesis and then inserted small N atoms into them by hydrothermal methods. Powder X-ray diffraction (XRD) analyses in Fig. 1b are conducted to confirm that the crystal structures of the catalysts are matched well to the standard Rh (PDF# 87-0714). The (111) peak at 41° shows a slight negative shift about 0.3°, indicating lattice expansion due to the introduction of N atoms into the interstitial sites of Rh crystal structure. The valence state and chemical composition of the catalyst surface were characterized by X-ray photoelectron spectroscopy (XPS). Fig. 1c depicts the high-resolution Rh 3d spectra of N-Rh/C, which can be separated into metallic peaks ( $\text{Rh}^0$  3d<sub>3/2</sub>, 312.1 eV;  $\text{Rh}^0$  3d<sub>5/2</sub>, 307.4 eV) and oxidized Rh species ( $\text{Rh}^{3+}$  3d<sub>3/2</sub>, 313.1 eV;  $\text{Rh}^{3+}$  3d<sub>5/2</sub>, 308.4

eV).<sup>30,31</sup> Compared with Rh/C, the  $\text{Rh}^0$  peaks exhibit 0.3 eV positive shift, indicating that the electron transport from Rh to N, resulted in electron-deficient state of Rh atoms. The N 1s XPS spectra (Fig. 1d) has two peaks at 397.9 and 399.9 eV, corresponding to N-Rh bond and pyrrolic N.<sup>32,33</sup> The atomic proportion of Rh and N in N-Rh/C is 16.58% and 2.97% respectively, according to the XPS results in Table S1. The transmission electron microscopy (TEM) images show uniformly dispersed nanoparticles and the average size is about 2.81 nm in Fig. 1e. Combined with the similar morphology and particle size of Rh/C (Fig. S1), the difference in activities caused by particle size is eliminated. The high-resolution STEM images prove that the lattice spacing in the (200) plane of N-Rh nanoparticles is 0.195 nm, and the lattice spacing in the (111) plane is 0.229 nm, which are slightly expanded compared with 0.190 nm and 0.219 nm in conventional Rh, confirming the successful introduction of N at the interstitial position of Rh nanoparticles. Corresponding fast Fourier transform (FFT) pattern is further confirmed (Fig. 1f).<sup>34</sup> Furthermore, the elemental distribution of the N-Rh nanoparticles was studied using HAADF-STEM energy-dispersive X-ray (EDX) mapping (Fig. 1g), in which the Rh and N are uniformly distributed. The line-





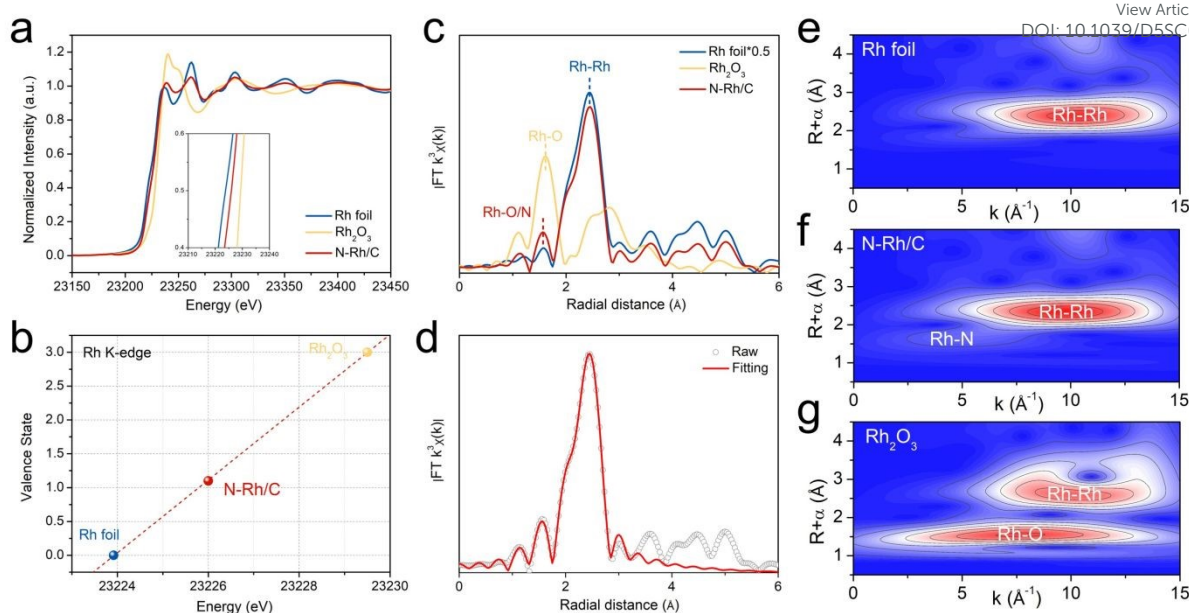


**Fig. 2** (a) Rh K-edge XANES spectra of the Rh foil, N-Rh/C and  $\text{Rh}_2\text{O}_3$  with the references. (b) Determination of Rh oxidation in N-Rh/C. (c) Fourier transform of EXAFS spectra for Rh. (d) EXAFS fitting curves in R space of N-Rh/C. Wavelet transforms for the  $k^3$ -weighted Rh K-edge EXAFS of Rh foil (e), N-Rh/C (f) and  $\text{Rh}_2\text{O}_3$  (g).

scan electron energy loss spectroscopy (EELS) spectra were collected across the N-Rh nanoparticle (Fig. S2), showing distinct Rh  $M_{3-2}$ -edge and N K-edge signals.

X-ray absorption structure (XAS) spectroscopy measurements were investigated to further obtain the local coordination environment of the N-Rh/C. Fig. 2a shows the normalized Rh K-edge XANES spectra of N-Rh/C. With Rh foil and  $\text{Rh}_2\text{O}_3$  as reference, the line of N-Rh/C displayed a positive shift, and the average valence of Rh in N-Rh/C is determined to be +1.1, which means that Rh transfers electrons outward (Fig. 2b).<sup>35</sup> The extended X-ray absorption fine structure (EXAFS) spectra of the N-Rh/C shows the local coordination environment around Rh sites in Fig. 2c, in which the peak at 1.5 Å belongs to the Rh-O/N bond, and the peak at 2.4 Å indicates the Rh-Rh bond. The quantitative least squares EXAFS fitting analysis obtained the local chelation parameters around the Rh sites, and the corresponding fitted structural parameters were shown in Fig. 2d and listed in Table S2. Two different local coordination structures of Rh-Rh coordination shell and Rh-O/N coordination shell for N-Rh/C with the average bond lengths of 2.45 and 1.56 Å, which show coordination numbers of 7.9 and 2.7, can reveal that N atoms inserted into the lattice gap of Rh successfully. The wavelet-transform (WT) corresponding to the Rh K-edge EXAFS (Fig. 2e-g) further verified the Rh-Rh and Rh-N bonds in N-Rh/C, further confirming the nitridation of Rh nanoparticles.

The electrocatalytic performance toward alkaline HOR of the obtained samples were evaluated with a standard three-electrode system in an  $\text{H}_2$ -saturated 0.1 M KOH electrolyte. As shown in Fig. 3a, the current density of N-Rh/C shows a significant enhancement compared with Rh/C and commercial Pt/C, manifesting the significance of interstitial nitrogen in improving the HOR activities. According to the simplified Butler-Volmer equation (Fig. S3), the micro-polarization region (-5 to 5

mV) further confirms improvement of performance. The influence of N-doping amount on the catalyst activity is studied by changing the input amount of urea. As shown in Fig. S4, N-Rh/C with an input amount of 240 mg urea has the best performance. Furthermore, in order to exclude the influence of  $\text{H}_2$  mass transport and obtain kinetic current densities ( $j^k$ ), the HOR polarization curves of N-Rh/C as a function of the rotation rate at rotation speeds from 625 to 2500 rpm were investigated to obtain the relevant kinetic parameters (Fig. S5), for which the increased plateau current density along with the elevated rotation rate indicates accelerated mass transport. The corresponding Koutecky-Levich plot was constructed, in which the  $j^{-1}$  exhibits a linear relationship with the  $\omega^{-1/2}$  (Fig. S5-S7).<sup>36</sup> The kinetic current densities ( $j^k$ ) of the HOR on the N-Rh/C, Rh/C, and Pt/C electrodes were extracted using the Koutecky-Levich equation. The corresponding Tafel plots of the samples are presented in Fig. 3b.<sup>37-39</sup> Based on the inductively coupled plasma atomic emission spectroscopy (ICP-AES) results in Table S3, the normalized mass activity denoted as  $j^{k,m}$  at the overpotential of 50 mV of the N-Rh/C is 1.04  $\text{mA } \mu\text{g}_{\text{Rh}}^{-1}$ , which is 8.0 and 2.7 times greater than those of the Rh/C (0.13  $\text{mA } \mu\text{g}_{\text{Rh}}^{-1}$ ) and Pt/C (0.38  $\text{mA } \mu\text{g}_{\text{Pt}}^{-1}$ ), respectively. Furthermore, the N-Rh/C also present the highest  $j^{0,m}$  among the tested samples (Fig. S8). The electrochemically active surface area (ECSAs) was tested by the Cu underpotential deposition ( $\text{Cu}_{\text{upd}}$ ) to investigate the intrinsic activities of different catalysts (Fig. S9). The ECSA normalized exchange current density ( $j^{0,s}$ ) was estimated. As shown in Fig. 3c, N-Rh/C unambiguously exhibited the highest  $j^{0,s}$  of 0.73  $\text{mA cm}^{-2}$ , which is approximately three times higher than those of Rh/C (0.27  $\text{mA cm}^{-2}$ ) and Pt/C (0.23  $\text{mA cm}^{-2}$ ). Furthermore, the exchange current density of N-Rh/C outperform most of the platinum-group metal (PGM)-based HOR catalysts in the previous reports (Fig. S10 and Table S4).



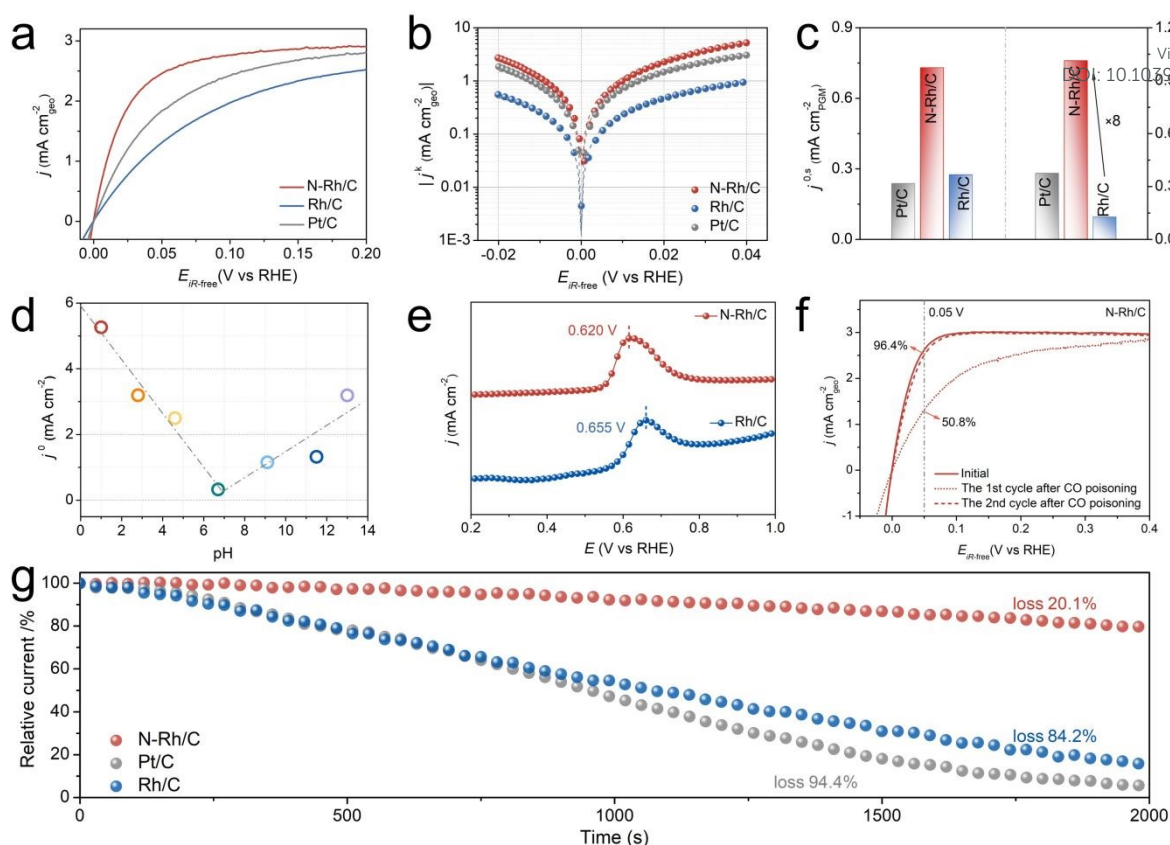


**Fig. 3** (a) HOR polarization curves of N-Rh/C, Rh/C, and Pt/C in  $\text{H}_2$ -saturated 0.1 M KOH. (b) Tafel plots derived from (a), normalized  $j^*$  by the Butler-Volmer fittings. (c) Comparison of the mass activities ( $j^m$ ) at 50 mV and the ECSA-normalized exchange current densities ( $j^{0.5}$ ) of N-Rh/C, Rh/C, and Pt/C. (d) Non-monotonously relation between  $j^0$  and the pH of N-Rh/C. (e) CO stripping curves of N-Rh/C and Rh/C. (f) HOR polarization curves before (solid line) and after (dashed line) a chronoamperometry test of N-Rh/C in  $\text{H}_2$ -saturated 0.1 M KOH solution. (g) I-t curves obtained at 0.1 V vs. RHE in 1000 ppm  $\text{CO}/\text{H}_2$ -saturated 0.1 M KOH solution.

In recent years, with continuous exploration and discoveries by previous studies regarding the pH effect involved in hydrogen oxidation reactions (HOR), it has been found that some catalysts exhibit inflection point behavior, that is, the apparent activity ( $j^0$ ) initially decreases and then increases as the pH of the electrolyte increases. This phenomenon not only challenges the traditional belief that higher alkalinity leads to slower HOR kinetics but also highlights the intensity of hydroxyl adsorption as a primary descriptor for HOR activity under alkaline conditions.<sup>40,41</sup> Therefore, further investigation into the activity optimization mechanism of N-Rh/C was conducted by measuring pH-universal HOR polarization curves (Fig. S11 and Table S5). As shown in Fig. 3d, when the pH  $\sim 7$ , the  $j^0$  of N-Rh/C abnormally increases. The same situation occurs at Rh/C, but it shows an abnormally increased  $j^0$  only when the pH  $\sim 8.2$  in Fig. S12. Moreover, CO stripping experiments indicated that the peak of CO oxidation for the N-Rh/C catalyst shifted negatively by 35 mV compared to that of Rh/C (Fig. 3e), suggesting a stronger binding affinity between N-Rh/C and  $\text{OH}^*$ .<sup>42</sup> The zeta potential experiments manifest the strengthened OHBE as well, on the basis of more negative charge of N-Rh/C (-25.76 mV) than Rh/C (-15.16 mV) in Fig. S13. The stability tests of the catalysts were carried out by conducting 1000 cyclic voltammetry (CV) measurements to test the stability of the catalyst. The polarization curve and CV curve (Fig. S14) of N-Rh/C did not attenuate significantly before and after stability

test, and the exchange current density could maintain 97.16%, which was better than Rh/C (Fig. S15), highlighting the excellent stability of N-Rh/C. In addition, the structure of the catalyst remains basically unchanged after stability test (Fig. S16). The N 1s XPS spectra after the stability test also shows the existence of the interstitial N in Fig. S17.

Limited by the means of hydrogen production, the hydrogen used at the anode side will inevitably contain trace CO impurities. The CO adsorbed on the catalyst active site compete with the intermediates  $\text{H}^*$  and  $\text{OH}^*$  involved in the HOR process, causing catalyst poisoning, resulting in reduced activity and even catalyst inactivation.<sup>43,17</sup> The CO resistance for the catalysts was evaluated by the HOR polarization curves before and after a chronoamperometry test under 1000 ppm  $\text{CO}/\text{H}_2$ . Compared with the initial curve without CO poisoning, in the first cycle curve after CO poisoning, the current density of N-Rh/C maintained 50.8% at 0.05 V, while Rh/C only remained 5.14% (Fig. 3f, S18), which indicates that the surface of N-Rh/C absorbed less CO and the adsorption capacity was weaker. As the electric potential increases, the adsorbed CO may oxidize/desorb with the adsorbed OH, resulting in reversible recovery of the poisoned active site.<sup>44</sup> As expected, in the second cycle curve at 0.05 V, the current density of N-Rh/C can recover to 96.4%, while Rh/C only recovers to 53.3%. Based on the above experimental phenomena, it can be reasonably inferred that N-Rh/C has the weaker CO adsorption



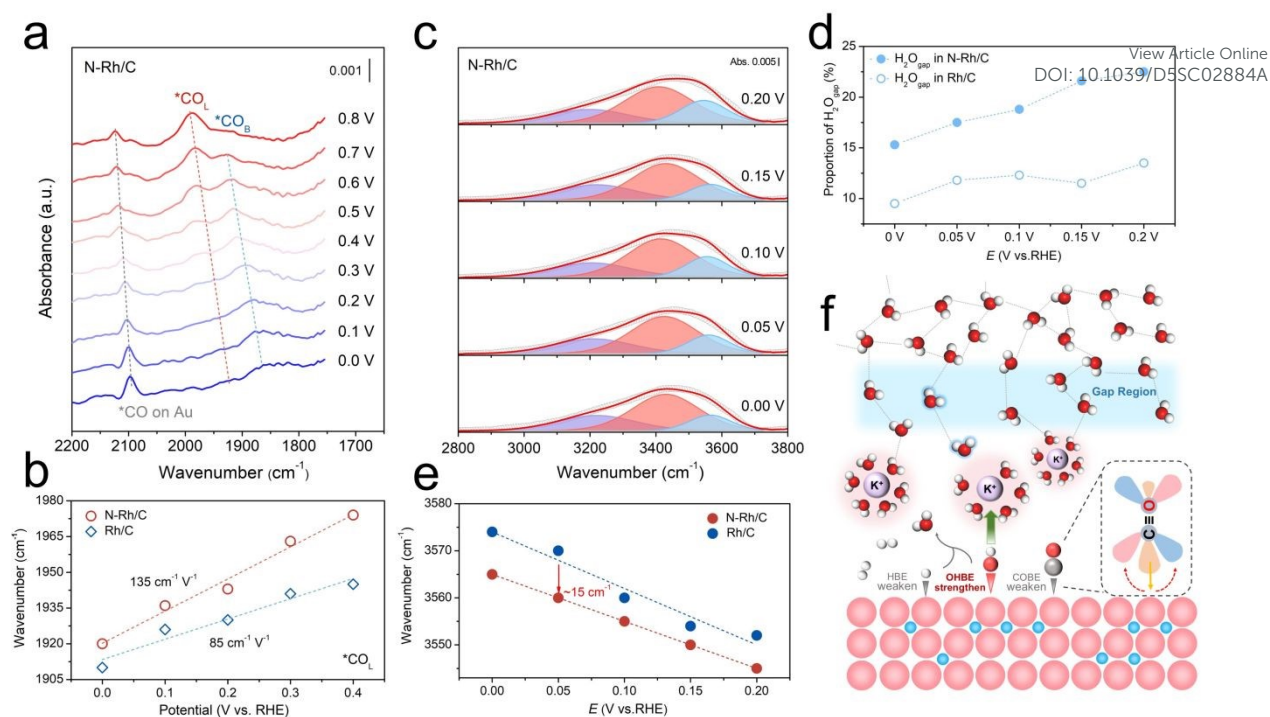


**Fig. 4** (a) In situ SEIRAS about CO adsorption state of the N-Rh/C. (b) Linear-bounded CO on N-Rh/C as a function of potential. (c) Deconvolution of the O-H stretching vibration features of in situ SEIRAS spectra. (d) Proportion of  $\text{H}_2\text{O}_{\text{gap}}$  from in situ SEIRAS spectra. (e) Comparison of the O-H stretching vibration frequencies of  $\text{H}_2\text{O}_{\text{gap}}$  of N-Rh/C and Rh/C from in situ SEIRAS spectra. (f) Schematic illustration of alkaline HOR and CO resistance.

capacity, and the enhanced OH adsorption releases the toxic active site, thus achieving excellent CO resistance. I-t curves in Fig. 3g are obtained by chronoamperometry tests at 0.1 V vs. RHE in 1000 ppm  $\text{CO}/\text{H}_2$ -saturated 0.1 M KOH solution. The current density of Rh/C and commercial Pt/C rapidly deactivate in 2000 s, while N-Rh/C can still maintain 70% at 4000 s, indicating the superior CO tolerance (Table S6).

Many studies have shown that the CO adsorption is related to the transfer of electrons from metal 4d to the CO  $2\pi^*$  orbital.<sup>45</sup> In general, the more electrons are transferred in reverse, the stronger the Rh-C bonds and the weaker the corresponding C-O bonds. Therefore, in situ SEIRAS can be used to determine the extent of electron back-donation and its effect on CO adsorption.<sup>46,47</sup> As shown in Fig. 4a and S19, SEIRAS of N-Rh/C and Rh/C were collected at the potential from 0 to 0.8 V in a CO-saturated 0.1 M KOH solution, and the peaks of  $\sim 2100\text{ cm}^{-1}$  could be attributed to the CO adsorbed on the Au film substrate. The CO adsorption on the catalyst is divided into two types due to its different state: bridge adsorption ( $\text{*CO}_B$ ) at around  $1850\text{ cm}^{-1}$  and linear adsorption ( $\text{*CO}_L$ ) at around  $1950\text{ cm}^{-1}$ , among which the adsorption of  $\text{*CO}_L$  is the main cause of catalyst poisoning. Firstly, compared with Rh/C, the peak strength of both  $\text{*CO}_B$  and  $\text{*CO}_L$  in N-Rh/C, are significantly reduced, indicating lower CO coverage on its surface, which indirectly reflects its weak CO adsorption. In addition, the blueshift of peaks occur with the incremental potentials, which are consistent with the decrease of back-donation from the Rh 4d to the CO  $2\pi^*$  orbitals, leading to the weakened CO adsorption. A function between the CO vibrational wavenumber and the applied potential was constructed in Fig. 4b and S20. At the

same potential, the absorption peak frequency of N-Rh/C is higher than Rh/C, indicating that its CO adsorption is weakened. Moreover, the higher stark tuning rates of  $\text{*CO}_B$  ( $105\text{ vs }101\text{ cm}^{-1}\text{ V}^{-1}$ ) (Fig. S16) and  $\text{*CO}_L$  ( $135\text{ vs }85\text{ cm}^{-1}\text{ V}^{-1}$ ) (Fig. 4b) for N-Rh/C indicate the decrease of CO coverage, which further proves that the CO adsorption is inhibited, and explains the strong tolerance of N-Rh/C to CO.

The interfacial water structure in the electrical double layer (EDL) on the catalyst surface can also be observed by in situ SEIRAS.<sup>48,49</sup> The O-H stretching vibration peak ( $2800\text{ cm}^{-1} - 3800\text{ cm}^{-1}$ ) of interfacial water can be deconvolved into three different types of water, namely, the water molecule located in the gap region ( $\text{H}_2\text{O}_{\text{gap}}$ ,  $\sim 3600\text{ cm}^{-1}$ ), the water molecule located above the interstitial region ( $\text{H}_2\text{O}_{\text{above-gap}}$ ,  $\sim 3400\text{ cm}^{-1}$ ) and the water molecule near the electrode surface ( $\text{K}\cdot\text{H}_2\text{O}$ ,  $\sim 3200\text{ cm}^{-1}$ ), in which the  $\text{H}_2\text{O}_{\text{gap}}$  can be used as an index to judge the connectivity of hydrogen bond network (H-bond network) (Fig. 4c and S21).<sup>25,50,51</sup> Compared with Rh/C, N-Rh/C has a higher proportion of  $\text{H}_2\text{O}_{\text{gap}}$  and it improves with the increase of applied potential (Fig. 4d). Upon analyzing the proportional changes of various types of interfacial water in Fig. S22, it was found that as the potential increased, the proportion of  $\text{K}\cdot\text{H}_2\text{O}$  decreased, the proportion of  $\text{H}_2\text{O}_{\text{gap}}$  increased, while that of  $\text{H}_2\text{O}_{\text{above-gap}}$  remained largely stable. Therefore, the enhanced OH adsorption on N-Rh/C can prompt more OH species to coordinate with  $\text{K}^+$ , causing them to release more free water into adjacent gap region to construct H-bond networks. Moreover, the O-H stretching bond of  $\text{H}_2\text{O}_{\text{gap}}$  moves  $\sim 15\text{ cm}^{-1}$  toward the lower wavenumber (Fig. 4e), indicating that the increased concentration of water in the gap region, which can





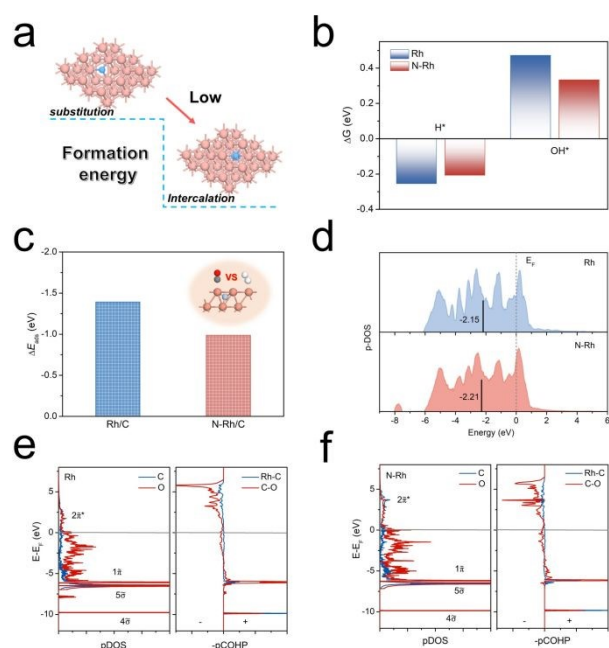


**Fig. 5** (a) The top view calculation models of N doped Rh in substituting Rh atom and intercalating into the Rh octahedral interspace. Rh and N atoms are denoted by pink and blue spheres. (b) Gibbs free energy schematic plot for the adsorption of  $H^*$  and  $OH^*$  on the surface of Rh and N-Rh. (c) The adsorption energy difference  $\Delta E_{ads}$  ( $E_{ads,CO} - E_{ads,H_2}$ ) of Rh and N-Rh. (d) The pDOS of Rh 4d orbitals in Rh and N-Rh. The pDOS and -pCOHP curves for CO adsorption on (e) Rh and (f) N-Rh surface.

further promote the H-bond network continuity. This further leads to abnormal behavior of the catalyst's activity at lower pH conditions - an earlier appearance of the inflection point. These phenomena represent that N-Rh/C has a better proton transport, and improves the reaction kinetics of alkaline HOR. Consequently, the function of interstitial N atoms achieves the enhancement of CO resistance and HOR activity by weakening CO adsorption but strengthening OHBE (Fig. 4f).

Carry out density functional theory (DFT) calculations to gain an in-depth understanding of the structure-adsorption relationship. Firstly, in order to prove that N atoms are more inclined to intercalate into the Rh octahedral interspace than to replace the Rh atoms, the corresponding structural model is calculated in Fig. 5a. The intercalation behavior has lower formation energy, indicating that its structure is more stable. This verifies the rationality of the N-Rh structure prepared in this work, and provides a basis for the subsequent DFT calculation.<sup>32,33</sup> As shown in Fig. S23, Rh (111) and N-Rh (111) models are constructed. According to calculate the charge density difference on Rh (111) before and after the introduction of interstitial N in Fig. S24, it can be determined that there is an obvious electronic interaction between the interstitial N and the surrounding Rh sites. Firstly, the adsorption energy of  $H^*$  and  $OH^*$ , the key intermediates involved in the alkaline HOR process, was calculated following the structural models shown in Fig. S25 and S26. N-Rh exhibits a Gibbs free energy for  $H^*$  ( $\Delta G_{H^*}$ ) of -0.206 eV, indicating weaker hydrogen binding strength compared to Rh (-0.254 eV) (Fig. 5b), which is consistent with the hydrogen underpotential deposition ( $H_{upd}$ )

findings from cyclic voltammetry (CV) experiments (Fig. S27).<sup>52,53</sup> The lower binding strength facilitates the rapid adsorption or desorption of H intermediates during the reaction, promoting their binding with other intermediates. The Gibbs free energy for  $OH^*$  ( $\Delta G_{OH^*}$ ) on N-Rh (0.333 eV) was significantly enhanced than that of Rh (0.472 eV) in Fig. 5b, which is conducive to the oxidation of  $H^*$  and  $CO^*$ .<sup>43,17</sup> Moreover, the enhancement of OHBE can promote the connectivity of the hydrogen bond network in the EDL and promote the reaction kinetics, which is the reason why the alkaline HOR activity of N-Rh/C is increased.<sup>50,51</sup> In addition, compared with Rh, the adsorption energy of  $CO^*$  on N-Rh is reduced (Fig. S28 and S29), which is consistent with the in situ SEIRAS results (Fig. 4a). Combined with the computational model and previous studies,  $CO^*$  and  $H^*$  compete for the same active site, so the adsorption strength of the two on the catalyst surface was compared. As shown in the Fig. 5c, the introduction of N atoms significantly reduced the difference in adsorption energy between  $CO^*$  and  $H^*$ , improved the adsorption competitiveness of  $H^*$ , thus promoted the CO-resistant ability of the catalyst. The projected partial density of state (pDOS) in Fig. 5d shows the position of d-band center ( $E_d$ ) of N-Rh further away from the Fermi level ( $E_f$ ), weakening the  $H^*$  adsorption and reducing the degree of the electron back-donation from Rh 4d to  $CO\ 2\pi^*$ .<sup>54,55</sup> In order to further explore the reason of the attenuated COBE/HBE but enhanced OHBE, by analyzing the computational models, it is found that  $CO^*/H^*$  tends to be adsorbed at the same site and  $OH^*$  at another site (Fig. S25, 26 and 28). According to calculate the charge density difference on Rh (111) before and after the introduction of interstitial N, the influence of interstitial N on the Rh site is nonhomogeneous. As shown in Fig. S30, the electron deficiency state around  $CO^*/H^*$  site reduces the degree of the electron back-donation from Rh 4d to  $CO\ 2\pi^*$  and shows the position of d-band center ( $E_d$ ) of N-Rh further away from the Fermi level ( $E_f$ ), weakening the CO adsorption, while electron accumulation around  $OH^*$  site led to the opposite adsorption result.<sup>56,57</sup> The Bader charge analysis also indicates that the  $CO^*/H^*$  sites tend to lose electrons and the OH sites tend to gain electrons.

By tracking the molecular orbital interactions between CO adsorbents and Rh active sites in different models, the reasons for inhibiting CO adsorption were explored in depth. Specifically, CO internal bonds and Rh-CO interactions on catalysts were revealed by C- and O- projected density of states (pDOS) and projected crystal orbital Hamilton population (pCOHP) (Fig. 5e and 5f). Compared with Rh, the  $2\pi^*$  orbital of CO on the N-Rh surface in a higher energy level and less occupied, indicating weaker CO adsorption and activation. In addition, the reduction of the occupied bond orbitals of Rh-C on the N-Rh relative to the Rh can be quantitatively obtained by integrating the projected crystal orbital Hamilton population (IpCOHP) (Table S7), which also confirms the reduction of CO adsorption.<sup>58-60</sup> The results of orbital analysis show that the filling of interstitial N atoms at the octahedral site of Rh can reduce the chemisorption of CO by inhibiting the electron back-donation from the Rh 4d to the  $CO\ 2\pi^*$  orbitals. Based on all the studies conducted, the interstitial N atoms have the capability



to modulate the electronic structure of the Rh sites, leading to an augmentation of OHBE and a decrease in both HBE and COBE (CO binding energy). These alterations collectively contribute to the enhancement of alkaline HOR activity and the promotion of CO tolerance.

## Conclusions

In summary, we demonstrated that interstitial N modified N-Rh/C nanoparticles can be used as highly efficient and CO-resistant catalyst for alkaline HOR, with the mass activity 8.0 and 2.7 times higher than Rh/C and commercial Pt/C. Density functional theory calculations manifest that the existence of interstitial N leads to an electron-losing state at the CO\*/H\* site, which causes the upshifted d-band center to weaken HBE and suppress electronic back-donation from Rh 4d to the CO 2 $\pi^*$  orbital, and an electron-gaining state at the OH\* site, thus optimizing the binding energies of multiple intermediates simultaneously. Meanwhile, the observed inflection point behavior reflects the importance of hydroxyl adsorption, and according to in situ SEIRAS, the optimization of hydrogen-bond network continuity caused by OHBE enhancement also confirmed the acceleration of HOR kinetics. This work not only provides a unique direction for the design of advanced metal-based catalysts, but also inspires the exploration of efficient catalysts involving multi-intermediate reactions.

## Author Contributions

JY, CY, YZ and QX performed the material synthesis and electrochemical tests. JY performed the DFT calculations. WL supervised the work. JY and WL wrote the manuscript.

## Conflicts of interest

There are no conflicts to declare.

## Acknowledgements

This work was financially supported by the National Natural Science Foundation of China (22272121, 21972107), and National Key Research and Development program of China (2021YFB4001200). The numerical calculations in this paper have been done on the supercomputing system in the Supercomputing center of Wuhan University. We thank the BL11B beamline in the Shanghai Synchrotron Radiation Facility (SSRF) for the XAFS measurements. We thank the Core Facility of Wuhan University for the measurements of ICP-AES and XPS. We also thank the Core Research Facilities of College of Chemistry and Molecular Sciences, and the Center for Electron Microscopy at Wuhan University for their substantial supports of TEM measurements.

## Notes and references

- 1 L. Schlapbach, A. Züttel, *Nature*, 2001, **414**, 353-358.
- 2 B. P. Setzler, Z. Zhuang, J. A. Wittkopf, Y. Yan, *Nat. Nanotechnol.*, 2016, **11**, 1020-1025. DOI: 10.1039/D5SC02884A
- 3 C. Gunathilake, I. Soliman, D. Panthi, P. Tandler, O. Fatani, N. A. Ghulamullah, D. Marasinghe, M. Farhath, T. Madhujith, K. Conrad, Y. Du, M. Jaroniec, *Chem. Soc. Rev.*, 2024, **53**, 10900-10969.
- 4 H. A. Gasteiger, N. M. Markovic, *Science*, 2009, **324**, 48-49.
- 5 N. Ramaswamy, S. Mukerjee, *Chem. Rev.*, 2019, **119**, 11945-11979.
- 6 X. Wu, N. Chen, H. A. Klok, Y. M. Lee, X. Hu, *Angew. Chem. Int. Ed.*, 2021, **61**, e202114892.
- 7 Y. Gao, Y. Yang, R. Schimmenti, E. Murray, H. Peng, Y. Wang, C. Ge, W. Jiang, G. Wang, F. J. DiSalvo, D. A. Muller, M. Mavrikakis, L. Xiao, H. D. Abruña, L. Zhuang, *PNAS*, 2022, **119**, e2119883119.
- 8 S. Zhu, X. Qin, F. Xiao, S. Yang, Y. Xu, Z. Tan, J. Li, J. Yan, Q. Chen, M. Chen, M. Shao, *Nat. Catal.*, 2021, **4**, 711
- 9 C. Yang, Z. Dai, J. Yue, G. Wang, W. Luo, *Chem. Sci.*, 2025, **16**, 5266-5274.
- 10 T. Wang, L.-Y. Li, L.-N. Chen, T. Sheng, L. Chen, Y.-C. Wang, P. Zhang, Y.-H. Hong, J. Ye, W.-F. Lin, Q. Zhang, P. Zhang, G. Fu, N. Tian, S.-G. Sun, Z.-Y. Zhou, *J. Am. Chem. Soc.*, 2022, **144**, 9292-6301.
- 11 R. Chaubey, S. Sahu, O. O. James, S. Maity, *Renewable and Sustainable Energy Rev.*, 2013, **23**, 443-462.
- 12 G. Huang, Y. Wu, Y. Li, S. Du, Q. Liu, M. Li, D. Zhang, Z. Jiang, S. Zhong, S. Lu, L. Tao, S. Wang, *Adv. Funct. Mater.*, 2025, **35**, 241535.
- 13 H.-R. Pan, T. Tang, Z. Jiang, L. Ding, C. Xu, J.-S. Hu, *J. Phys. Chem. Lett.*, 2024, **15**, 3011-3022.
- 14 F. Gao, S. Liu, J. Ge, X. Zhang, L. Zhu, Y. Zheng, Y. Duan, S. Qin, W. Dong, X. Yu, R. Bao, P. Yang, Z. Niu, Z. Ding, W. Liu, S. Lan, M. Gao, Y. Yan, S. Yu, *Nat. Catal.*, 2022, **5**, 993-1005.
- 15 B. Zhang, B. Zhang, G. Zhao, J. Wang, D. Liu, Y. Chen, L. Xia, M. Gao, Y. Liu, W. Sun, H. Pan, *Nat. Commun.*, 2022, **13**, 5894.
- 16 X. Wang, Y. Tong, W. Feng, P. Liu, X. Li, Y. Cui, T. Cai, L. Zhao, Q. Xue, Z. Yan, X. Yuan, W. Xing, *Nat. Commun.*, 2023, **14**, 3767.
- 17 Y. Zhou, Z. Xie, J. Jiang, J. Wang, X. Song, Q. He, W. Ding, Z. Wei, *Nat. Catal.*, 2020, **3**, 454-462.
- 18 P. Wang, Y. Yang, W. Zheng, Z. Cheng, C. Wang, S. Chen, D. Wang, J. Yang, H. Shi, P. Meng, P. Wang, H. Tong, J. Chen, Q. Chen, *J. Am. Chem. Soc.*, 2023, **145**, 27867-27876.
- 19 Y. K. Feng, S. G. Lu, L. H. Fu, F. L. Yang and L. G. Feng, *Chem. Sci.*, 2024, **15**, 2123-2132.
- 20 N. Acerbi, S. C. E. Tsang, G. Jones, S. Golunski, P. Collier, *Angew. Chem., Int. Ed.*, 2013, **52**, 7737-7741.
- 21 T. He, W. Wang, F. Shi, X. Yang, X. Li, J. Wu, Y. Yin, M. Jin, *Nature*, 2021, **598**, 76-81.
- 22 Z. Xia, S. Guo, *Chem. Soc. Rev.*, 2019, **48**, 3265-3278.
- 23 L. Wei, N. Fang, F. Xue, S. Liu, W.-H. Huang, C.-W. Pao, Z. Hu, Y. Xu, H. Geng, X. Huang, *Chem. Sci.*, 2024, **15**, 3928-3935.
- 24 F. Yang, X. Bao, P. Li, X. Wang, G. Cheng, S. Chen, W. Luo, *Angew. Chem., Int. Ed.*, 2019, **58**, 14179-14183.
- 25 P. Li, Y. Jiang, Y. Hu, Y. Men, Y. Liu, W. Cai, S. Chen, *Nat. Catal.*, 2022, **5**, 900-911.
- 26 Y. Li, C.-K. Peng, H. Hu, S.-Y. Chen, J.-H. Choi, Y.-G. Lin, J.-M. Lee, *Nat. Commun.*, 2022, **13**, 1143.
- 27 T. Chen, I. Ellis, T. J. N. Hooper, E. Liberti, L. Ye, B. T. W. Lo, C. O'Leary, A. A. Sheader, G. T. Martinez, L. Jones, P.-L. Ho, P. Zhao, J. Cookson, P. T. Bishop, P. Chater, J. V. Hanna, P. Nellist, S. C. E. Tsang, *J. Am. Chem. Soc.*, 2019, **141**, 19616-19624.
- 28 R. Guo, Q. Chen, X. Li, Y. Liu, C. Wang, W. Bi, C. Zhao, Y. Guo, M. Jin, *J. Mater. Chem. A*, 2019, **7**, 4714-4720.
- 29 T. Chen, C. Foo, S. C. Edman Tsang, *Chem. Sci.*, 2021, **12**, 517-532.
- 30 Y. Zhang, G. Li, Z. Zhao, L. Han, Y. Feng, S. Liu, B. Xu, H. Liao, G. Lu, H. L. Xin, X. Huang, *Adv. Mater.*, 2021, **33**, 2105049;





- 31 H. Huang, K. Liu, F. Yang, J. Cai, S. Wang, W. Chen, Q. Wang, L. Fu, Z. Xie, S. Xie, *Angew. Chem., Int. Ed.*, 2023, **62**, e202315752.
- 32 M. Xie, B. Zhang, Z. Jin, P. Li, G. Yu, *ACS Nano*, 2022, **16**, 13715
- 33 Y. Zheng, B. Zhang, T. Ma, R. Yan, W. Geng, Z. Zeng, Y. Zhang, S. Li, *Small*, 2023, **20**, 2307405.
- 34 Y. Guo, X. Yang, X. Liu, X. Tong, N. Yang, *Adv. Funct. Mater.*, 2022, **33**, 2209134.
- 35 J. Hu, X. Wang, H. Liu, H. Li, Yi. Zhou, M. Liu, C. Wang, M. Li, Y. Tang, G. Fu, *Chem. Sci.*, 2025, **16**, 1837-1848.
- 36 L. Wang, Z. Xu, C. H. Kuo, J. Peng, F. Hu, L. Li, H. Y. Chen, J. Wang, S. Peng, *Angew. Chem., Int. Ed.*, 2023, **62**, e202311937.
- 37 S. Wang, L. Fu, H. Huang, M. Fu, J. Cai, Z. Lyu, Q. Wang, Q. Kuang, Z. Xie, S. Xie, *Adv. Funct. Mater.*, 2023, **33**, 2304125.
- 38 H. Shi, Y. Yang, P. Meng, J. Yang, W. Zheng, P. Wang, Y. Zhang, X. Chen, Z. Cheng, C. Zong, D. Wang, Q. Chen, *J. Am. Chem. Soc.*, 2024, **146**, 16619-16629.
- 39 Z. Huang, R. Lu, Y. Zhang, W. Chen, G. Chen, C. Ma, Z. Wang, Y. Han, W. Huang, *Adv. Funct. Mater.*, 2023, **33**, 2306333.
- 40 Y. Jin, X. Fan, W. Cheng, Y. Zhou, L. Xiao, W. Luo, *Angew. Chem., Int. Ed.*, 2024, **63**, e202406888.
- 41 P. Han, X. Yang, L. Wu, H. Jia, J. Chen, W. Shi, G. Cheng, W. Luo, *Adv. Mater.*, 2024, **36**, 2304496.
- 42 J. Fang, H. Wang, Q. Dang, H. Wang, X. Wang, J. Pei, Z. Xu, C. Chen, W. Zhu, H. Li, Y. Yan, Z. Zhuang, *Nat. Commun.*, 2024, **15**, 4236.
- 43 Y. C. Hou, T. Shen, K. Hu, X. Wang, Q. N. Zheng, J. B. Le, J. C. Dong, J. F. Li, *Angew. Chem., Int. Ed.* 2024, **63**, e202402496.
- 44 C. Yang, G. Wang, J. Yue, Z. Dai, W. Luo, *ACS Catal.*, 2024, **15**, 869-876.
- 45 B. Cai, X. Chen, L. Wang, H. Fu, *ACS Catal.*, 2024, **14**, 13602-13629.
- 46 Y. Dong, Z. Zhang, W. Yan, X. Hu, C. Zhan, Y. Xu, X. Huang, *Angew. Chem. Int. Ed.*, 2023, **62**, e202311722
- 47 C. Jin, Y. Liao, A. Zhang, S. Zhao, R. Wang, J. Li, H. Tang, *Nano Energy*, 2024, **122**, 109305.
- 48 Q. Sun, N. J. Oliveira, S. Kwon, S. Tyukhtenko, J. J. Guo, N. Myrthil, S. A. Lopez, I. Kendrick, S. Mukerjee, L. Ma, S. N. Ehrlich, J. Li, W. A. Goddard, Y. Yan, Q. Jia, *Nat. Energy*, 2023, **8**, 859-869.
- 49 K. Zhao, X. Chang, H. S. Su, Y. Nie, Q. Lu, B. Xu, *Angew. Chem., Int. Ed.*, 2022, **61**, e202207197.
- 50 Y. H. Wang, Y. Yang, F. Y. Gao, X. L. Zhang, L. Zhu, H. K. Yan, P. Yang, M. R. Gao, *Angew. Chem., Int. Ed.*, 2024, **63**, e202407613
- 51 J. Yue, Y. Li, C. Yang, W. Luo, *Angew. Chem., Int. Ed.*, 2024, **64**, e202415447.
- 52 M. Ma, G. Li, W. Yan, Z. Wu, Z. Zheng, X. Zhang, Q. Wang, G. Du, D. Liu, Z. Xie, Q. Kuang, L. Zheng, *Adv. Funct. Mater.*, 2022, **12**, 2103336;
- 53 J. Zheng, W. Sheng, Z. Zhuang, B. Xu, Y. Yan, *Sci. Adv.* 2016, **2**, e1501602.
- 54 M.-W. Gu, H. H. Peng, I. W. P. Chen, C.-h. Chen, *Nat. Mater.*, 2021, **20**, 658-664.
- 55 Y. Wan, W. Wei, S. Ding, L. Wu, H. Qin, X. Yuan, *Adv. Funct. Mater.* 2024, **35**, 2414554.
- 56 T. He, W. Wang, F. Shi, X. Yang, X. Li, J. Wu, Y. Yin, M. Jin, *Nature*, 2021, **598**, 76-81.
- 57 F. Tian, S. Geng, M. Li, L. Qiu, F. Wu, L. He, J. Sheng, X. Zhou, Z. Chen, M. Luo, H. Liu, Y. Yu, W. Yang, S. Guo, *Adv. Mater.*, 2025, 2501230.
- 58 Z. Yang, W. Lai, B. He, J. Wang, F. Yu, Q. Liu, M. Liu, S. Zhang, W. Ding, Z. Lin, H. Huang, *Adv. Funct. Mater.*, 2023, **13**, 2300881.
- 59 L. Foppa, C. Copéret, A. Comas-Vives, *J. Am. Chem. Soc.*, 2016, **138**, 16655-16668.
- 60 L. Lin, S. Yao, R. Gao, X. Liang, Q. Yu, Y. Deng, J. Liu, M. Peng, Z. Jiang, S. Li, Y.-W. Li, X.-D. Wen, W. Zhou, D. Ma, *Nat. Nanotechnol.*, 2019, **14**, 354-361.



- The data supporting this article have been included as part of the Supplementary Information.

